Check for updates

VOX supported on TiO2–Ce0.9Zr0.1O2 core–shell structure catalyst for NH3-SCR of NO

Lvesheng Sun, [ID] [a] Shunxin Cao,[a] Yun Huang,[a] Yiming Zhang,[a] Youhong Xiao,[b] Guojun Dong [ID] *[a] and Yu Su*[c]

In this experiment, a $TiO_2–Ce_{0.9}Zr_{0.1}O_2$ support with core–shell structure was successfully prepared by a precipitation method and $VO_X/TiO_2–Ce_{0.9}Zr_{0.1}O_2$ catalyst was prepared by an impregnation method, and the catalyst was used to catalyze the NH₃-SCR of NO. Based on the results of HRTEM, XRD, BET, H₂-TPR, NH₃-TPD, XPS, Py-IR, it was speculated that due to the interaction between TiO_2 and $Ce_{0.9}Zr_{0.1}O_2$, more oxygen vacancies and Ce^{3+} are generated, which are beneficial to the existence of low-valence V by electron transfer between high valence state V and Ce^{3+} and increase the acidic sites on the catalyst surface. The catalytic activity (>97%) of the $VO_X/TiO_2–Ce_{0.9}Zr_{0.1}O_2$ catalyst is superior to the current commercial catalyst ($V_2O_5–WO_3/TiO_2$) and has a higher N₂ selectivity (>97.5%) at 40 000 h⁻¹ GHSV and 250–400 °C.

Introduction

Nitrogen oxides (NO$_X$) cause serious environmental pollution. The technology of selective catalytic reduction (SCR) of NO$_X$ with NH₃ has been widely used to reduce pollution caused by NO$_X$. A lot of research work on SCR catalysts has been carried out.[1–4] But the most widely used catalyst is still $V_2O_5–WO_3(MoO_3)/TiO_2$ catalyst.[5,6] The wide application of this catalytic system benefits from its reasonable cost and high NO conversion. However, these catalysts still have some disadvantages such as narrow temperature windows of activity (300–400 °C) and poor catalytic activity in low temperature. Although many known SCR catalysts have relatively high NO conversion in a wider temperature range,[7,8] their selectivity, stability, and resistance to water and sulfur are not excellent. On the other hand, the production costs of catalysts with the above advantages may be greatly increased, making it difficult to achieve industrial production.

For two decades, CeO₂ has attracted more attention in the catalytic field due to its excellent ability to store and release oxygen as a result of the efficient change of Ce valence between +3 and +4.[9] The earliest application of CeO₂ in cleaning flue gases is mainly to deal with automobile exhaust as the three-way catalyst (TWC) in the presence of noble metals such as Rh, Pt and Pd. In order to further expand the application of CeO₂,

a large number of modification studies have been performed. Using the isovalent metal cations of smaller diameter to prepare solid solution by co-precipitation is one of the most common methods. Studies show that these Ce-based solid solutions have great potential for deNO$_X$.[10–14] Thanh Huyen Vuong and co-workers have investigated the relations between structural properties and catalytic performance in $VO_X/Ce_xTi_{1−x}O_2$ and $VO_X/Ce_xZr_{1−x}O_2$ catalysts, respectively.[15,16] The results indicates that VO$_X$ sites effectively attach to the support surface and the redox properties of the materials governs catalytic activity rather than Lewis and Brønsted surface acidic sites in this catalytic system. All above mentioned researches reveal the importance of oxygen mobility in catalytic reactions. Li et al.[17] prepared $CeO_2–WO_3/TiO_2$ by impregnation method and confirmed that CeO₂ is favorable to keep more acid sites and enhanced NO reduction in NH₃-SCR reaction compared with $V_2O_5–WO_3/TiO_2$. Li et al.[18] prepared a $CeO_2–MnO_X$ catalyst with a core–shell structure and it exhibits relatively good NO conversion in the presence of SO₂ on account of the fact that CeO₂ shell prevents the active sites of MnO$_X$ from being poisoned.

The SCR catalytic activity of $V_2O_5–WO_3(MoO_3)/TiO_2$ mainly stems from the adsorption of NH₃ by acidic sites possessed by highly dispersed V species on the TiO₂ surface, forming Bronsted-NH₃ and further reacting with NO in gas phase.[19,20] Differently, the Mars-van Krevelen mechanism of Ce-based solid solution catalyst has been clearly clarified.[15,16] We expect that adding this structure to traditional catalysts in another way can bring different effects and further optimize this catalytic system. In this work, the core–shell structure carrier of TiO₂ and $Ce_{0.9}Zr_{0.1}O_2$ was prepared by precipitation method, and loaded VO$_X$ on the carrier by impregnation method. Combined with the results of XRD, BET, H₂-TPR, NH₃-TPD, Py-IR, HRTEM and XPS,

[a]College of Materials Science and Chemical Engineering, Key Laboratory of Superlight Materials and Surface Technology of Education Ministry, Harbin Engineering University, 150001 Harbin, Heilongjiang, P. R. China. E-mail: dgj1129@163.com

[b]College of Power and Energy Engineering of Harbin Engineering University, 150001 Harbin, Heilongjiang, P. R. China

[c]School of Chemistry, Chemical Engineering and Materials of Heilongjiang University, 150080, Harbin, Heilongjiang, P. R. China. E-mail: 2003086@hlju.edu.cn

the reasons for the high activity and thermal stability of the catalyst are explained.

Experimental

Chemical reagents

$Ce(NO_3)_3 \cdot 6H_2O$ (Analytical Reagent) was purchased from Tianjin Guangfu Fine Chemical Research Institute. $Zr(NO_3)_4 \cdot 5H_2O$ (Analytical Reagent) was purchased from Tianjin Fuchen Chemical Reagents Factory. Nano titanium dioxide (Analytical Reagent) was purchased from Tianjin Guangfo Materials Co., Ltd. Ammonium metavanadate (Analytical Reagent) was purchased from Tianjin Zhiyuan Chemical Reagent Co., Ltd. Citric acid (Analytical Reagent) was purchased from Tianjin Dongli District Tianda Chemical Reagent Factory.

Catalysts preparation

$TiO_2–Ce_{0.9}Zr_{0.1}O_2$ support were prepared by precipitation method. 0.0225 M of cerium nitrate $(Ce(NO_3)_3 \cdot 6H_2O)$ and 0.0025 M of zirconium nitrate $(Zr(NO_3)_4 \cdot 5H_2O)$ were completely dissolved in an appropriate amount of deionized water, respectively. Then, the resulting solutions were mixed at room temperature for 10 min. 0.025 M TiO_2 powder was subsequently suspended in the mixed solution under vigorous stirring and the obtained mixture kept stirring for 1 h at room temperature, then heated to 80 °C to evaporate part of the water. When the mixture was slightly viscous, the ammonia water was added under stirring until pH = 10, and metal ions were precipitated on the surface of TiO_2. After the mixture was stirred at room temperature for 1 h, the obtained solution was aged at 70 °C for 5 h in the blast drying oven. Then, the precipitate was filtered and washed with deionized water. Finally, the obtained product was dried at 120 °C for 12 h and subsequently calcined in air at 500 °C for 4 h.

$VO_X/TiO_2–Ce_{0.9}Zr_{0.1}O_2$ $(VO_X/TiO_2, VO_X/Ce_{0.9}Zr_{0.1}O_2)$ catalyst with 3 wt% V_2O_5 loaded was prepared by wet impregnation. 0.195 g of the ammonium metavanadate (NH_4VO_3) was dissolved in 60 mL citric acid solution (10 wt% $C_6H_8O_7 \cdot H_2O$). 4.85 g of the $TiO_2–Ce_{0.9}Zr_{0.1}O_2$ $(TiO_2, Ce_{0.9}Zr_{0.1}O_2)$ powder was suspended in vanadium-containing solution and the obtained mixture kept stirring for 1 h then heated to 100 °C to evaporate the excess water completely. The obtained product was further dried at 120 °C for 12 h and subsequently calcined in air at 400 °C for 3 h.

NH3-SCR activity test

The SCR activity tests were conducted in a fixed-bed quartz reactor with 250 mm length and 8 mm internal diameter 0.3 mL (400 mg) catalyst with 40–60 mesh size were used for all tests. The typical reactant gas contained: 1000 ppm NO, 1000 ppm NH_3, 3%O_2 and balance Ar. The total gas flow rate was 200 mL min^{-1} and regulated by mass flow controllers (Sevenstar D08 series Flow Readout Boxed, Beijing Sevenstar Electronics Co., Ltd., Beijing, China), corresponding to the gas hourly space velocity (GHSV) of about 40 000 h^{-1}. NO, N_2, NH_3, NO_2 and N_2O outlet concentration were analyzed by the ThermoStar Gas

Analysis System GSD320 analyzer (Pfeiffer Vacuum GmbH, Berlin, Germany). Activity data was recorded with a temperature gradient of 50 °C in the range of 100 °C −450 °C. The NO conversion (C_{NO}) and N_2 selectivity (S_{N_2}) are calculated as following equations:

$$C_{NO} = \frac{[NO]_{in} - [NO]_{out}}{[NO]_{in}} \times 100\%$$

$$S_{N_2} = \left\{ 1 - \frac{2[N_2O]_{out} + [NO_2]_{out}}{[NO]_{in} - [NO]_{out} + [NH_3]_{in} - [NH_3]_{out}} \right\} \times 100\%$$

where $[NO]_{in}$ and $[NH_3]_{in}$ represent the inlet concentration of NO and NH_3. The $[NO]_{out}$, $[NH_3]_{out}$, $[NO_2]_{out}$ and $[N_2O]_{out}$ represent the outlet concentration of NO, NH_3, NO_2 and N_2O.

Catalyst characterization

X-ray diffraction (XRD) powder patterns were recorded by a D/MAX-3A Auto X-ray diffractometer (Rigaku Corporation, Tokyo, Japan) with Cu Kα radiation ($\lambda = 1.5418$ Å, 40 kV, 40 mA). The diffraction patterns were taken in the 2θ range of 10–80° at a scan speed of 10° min^{-1}.

HRTEM were recorded by FEI Talos F200X G2 electron microscope (PHILIPS, Amsterdam, The Netherlands).

The pore structure and specific surface area (SSA) of the catalyst were measured using a SSA-6000 pore and surface area analyzer manufactured by Beijing Builder Electronic Instrument Co., Ltd., and calculated by the Brunauer–Emmett–Teller (BET) and the Barrett–Joyner–Halenda (BJH) method. The sample was pretreated under vacuum at 200 °C for 2 h, the adsorption medium was N_2 with He was carrier. The inlet pressure of the system was 0.3 MPa.

In situ Py-IR was performed on a Fourier transform infrared spectrometer (Nicolet 6700, Thermo Fisher Scientific, Waltham, MA, America) equipped with a smart collector and MCT detector cooled by liquid N_2, collecting 32 scans with a resolution of 4 cm^{-1}. The catalysts were firstly pretreated in Ar at 250 °C for 40 min, then cooled down to 20 °C. Then, the background spectrum was recorded with the flowing of Ar and subtracted from the sample spectrum. Subsequently, the gaseous pyridine were introduced to the catalyst for 30 min, and then flushed with Ar for 10 min. The spectra were normally collected at temperature ranging from room temperature to 350 °C.

H_2-TPR was performed by PCA-1200 chemical adsorption analyzer and 0.05 g sample was pretreated in Ar (30 mL min^{-1}) at 250 °C for 40 min and then heated up to 800 °C at a rate of 10 °C min^{-1} under 5 vol% H_2/Ar.

NH_3-TPD was performed by PCA-1200 chemical adsorption analyzer and 0.05 g sample was pretreated in Ar (30 mL min^{-1}) at 250 °C for 40 min and then the NH_3 was adsorbed at room temperature for 10 min. It was purged in Ar at 100 °C for 1 h, then cooled down to the room temperature and finally heated to 650 °C at a rate of 10 °C min^{-1} under Ar.

X-ray photoelectron spectra were obtained with K-Alpha spectrometer (Thermo Fisher Scientific, Waltham, MA,

America) using Al Kα (1486.7 eV) radiation as the excitation source with a precision of ±0.3 eV. All binding energies were referenced to the C 1s line at 284.8 eV.

Results and discussion

The HRTEM analysis

High-resolution transmission electron microscopy (HRTEM) was used to characterize the $VO_X/TiO_2-Ce_{0.9}Zr_{0.1}O_2$ catalysts (Fig. 1). The catalyst was well dispersed and a relatively obvious core–shell structure was observed (Fig. 1a and b). The 3.5 nm $Ce_{0.9}Zr_{0.1}O_2$ shell is coated on the outside of the TiO_2 core the magnified portion of the core–shell structure in Fig. 1c was shown in Fig. 1d. The lattice fringes of $VO_X/TiO_2-Ce_{0.9}Zr_{0.1}O_2$ display inter planar spacings of 0.312 nm and 0.189 nm in the particle, which match well with those of the (111) plane of cubic $Ce_{0.9}Zr_{0.1}O_2$ (CeO_2) and (200) plane of anatase TiO_2, respectively.[21] It needs to note that no lattice fringes attributed to VO_X were observed. In order to verify the distribution of the elements, the catalyst was subjected to mapping (Fig. 1e), and the distribution of the V element is shown in Fig. 1f. The V element is evenly distributed on the support surface, also indicating its existence.
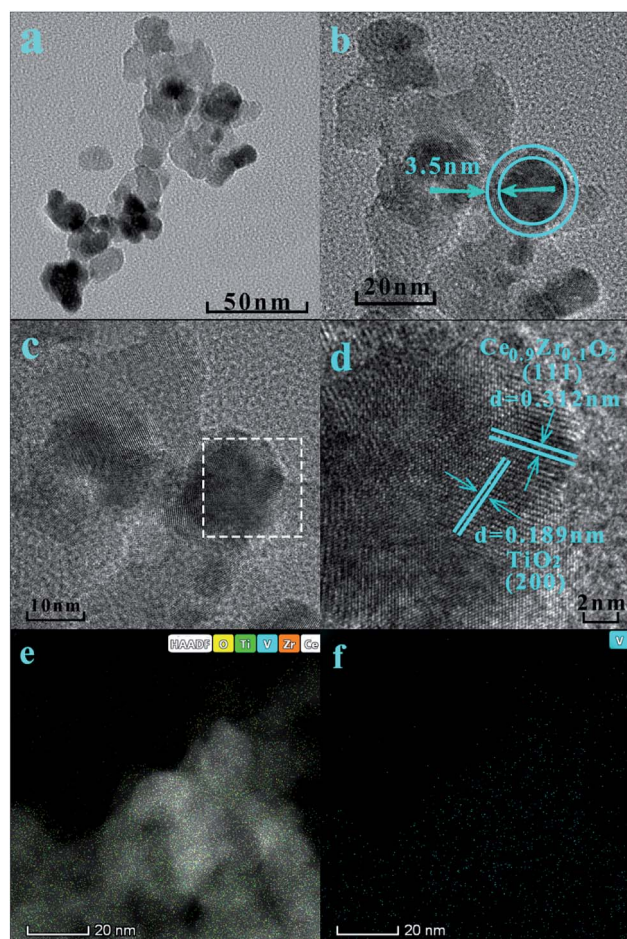

Fig. 1 HRTEM images (a–d) and V element mapping of $VO_X/TiO_2-Ce_{0.9}Zr_{0.1}O_2$ (e and f).

XRD and BET analysis

Fig. 2 is the XRD comparison of the support and the VO_X supported catalyst. The diffraction pattern for catalyst containing TiO_2 has six peaks at 25.28°, 37.80°, 48.05°, 53.89°, 55.06° and 62.69° corresponding to (101), (004), (200), (105), (211), and (204) crystal faces of anatase TiO_2 (PDF#21-1272), respectively.[22] The diffraction peak at 28.55°, 33.08°, 47.48°, and 56.34° of the catalyst containing $Ce_{0.9}Zr_{0.1}O_2$ corresponds to (111), (200), (220), (311) of cubic CeO_2 (PDF#43-1002), respectively.[23,24] It is worth noting that in the XRD spectrum, no diffraction peaks attributed to ZrO_2 were observed, which indicates that the size of Zr ion (0.084 nm) is significantly smaller than that of Ce ion (0.097 nm), the addition of Zr^{4+} does not destroy the lattice structure of CeO_2 itself meaning that the formation of a CeO_2–ZrO_2 solid solution.[25,26] This is consistent with the result that the lattice fringes belonging to the (111) crystal plane having a crystal face spacing of 0.312 nm in CeO_2 were observed in HRTEM.

For $TiO_2-Ce_{0.9}Zr_{0.1}O_2$ and $VO_X/TiO_2-Ce_{0.9}Zr_{0.1}O_2$, although TiO_2 has a larger specific surface area (SSA), the diffraction peaks attributed to $Ce_{0.9}Zr_{0.1}O_2$ and TiO_2 with a molar ratio of 1 : 1 indicate, that $Ce_{0.9}Zr_{0.1}O_2$ is not simply dispersed on TiO_2 surface.[27] Instead, it crystallizes on the surface of TiO_2 core to form a shell structure or forms incomplete coating on the surface of TiO_2 core. Interestingly, due to the load of VO_X, the diffraction peak intensity of the $VO_X/TiO_2-Ce_{0.9}Zr_{0.1}O_2$ catalyst is enhanced, and the peak shape becomes sharper, which may be that the loading of VO_X weakens the interaction between $Ce_{0.9}Zr_{0.1}O_2$ and TiO_2, and increases the degree of crystallization of the $TiO_2-Ce_{0.9}Zr_{0.1}O_2$ core–shell structure. However, compared with $Ce_{0.9}Zr_{0.1}O_2$ and $VO_X/Ce_{0.9}Zr_{0.1}O_2$, the loaded VO_X has no significant effect on $Ce_{0.9}Zr_{0.1}O_2$. From the partial comparison of XRD, we speculate that for $TiO_2-Ce_{0.9}Zr_{0.1}O_2$, the loaded VO_X complements the oxygen vacancies in $Ce_{0.9}Zr_{0.1}O_2$, and the cell of $Ce_{0.9}Zr_{0.1}O_2$ is more complete, and the crystallinity of the sample is higher.[28,29] For $VO_X/Ce_{0.9}Zr_{0.1}O_2$, the oxygen vacancies cannot be replenished due to the lack of interaction between TiO_2 and $Ce_{0.9}Zr_{0.1}O_2$, and the crystallinity and unit cell distortion are not significantly improved. For the
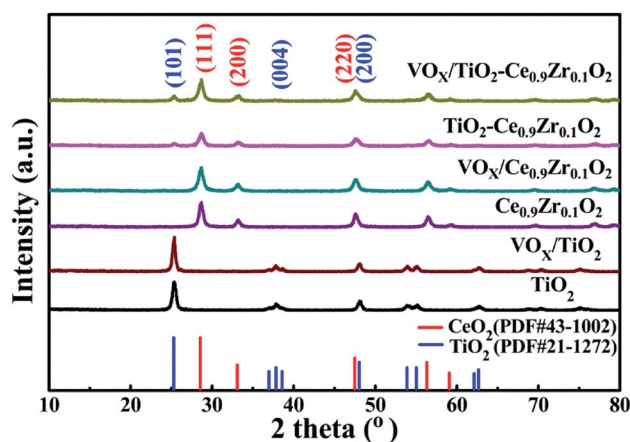

Fig. 2 XRD spectrum of VO_X supported catalysts and carriers.

VO_X-loaded catalyst, the VO_X loading mass percentage is small, the diffraction peak attributed to VO_X cannot be observed, indicating that the VO_X is highly dispersed on the core–shell structure carrier or in an amorphous form.[30,31] This is consistent with the fact that the lattice fringe attributed to VO_X was not observed in the HRTEM of VO_X/TiO_2–$Ce_{0.9}Zr_{0.1}O_2$.

It is worth mentioned that TiO_2 has the largest specific surface area in all samples (Table 1), the loading of VO_X or the formation of core–shell structure with $Ce_{0.9}Zr_{0.1}O_2$ will cause the specific surface area to decrease. However, for $Ce_{0.9}Zr_{0.1}O_2$, the loading of VO_X and the formation of a core–shell structure with TiO_2 will increase the specific surface area. This results in a core–shell structure having a specific surface area between $Ce_{0.9}Zr_{0.1}O_2$ and TiO_2. Combining the pore volume (PV) and the pore size (PS) information, we can speculate that VO_X and $Ce_{0.9}Zr_{0.1}O_2$ enter the pores of TiO_2 during the formation process of VO_X/TiO_2 and TiO_2–$Ce_{0.9}Zr_{0.1}O_2$, resulting in a decrease in specific surface area, pore volume and pore size. The cerium–zirconium solid solution constituting the core–shell structure is different from pure $Ce_{0.9}Zr_{0.1}O_2$ in terms of specific surface, pore volume and pore size. It is a shell formed by spreading on the surface of TiO_2. The specific surface area is relatively large compared with the simple $Ce_{0.9}Zr_{0.1}O_2$, and this can provide more acidic sites. Due to the interaction between TiO_2 and $Ce_{0.9}Zr_{0.1}O_2$, the pores formed by $Ce_{0.9}Zr_{0.1}O_2$ also change. When VO_X is loaded, it is arranged on the surface of the pure $Ce_{0.9}Zr_{0.1}O_2$ sample, and some special pores may be formed to increase the specific surface area. For TiO_2–$Ce_{0.9}Zr_{0.1}O_2$, VO_X is not only arranged on the surface, but also may enter certain special channels. Therefore, the specific surface area, pore volume and pore size are reduced.

H$_2$-TPR analysis

The redox performance of several catalysts was analyzed by H$_2$-TPR technique, and the spectrums are illustrated in Fig. 3. According to Chen's report, the reduction ability of the anatase TiO_2 phase is weak. There is no obvious reduction peak in the range of 50–800 °C, and the reduction performance of V_2O_5 is strong, and there is obvious reduction peak in the range of 50–800 °C.[32] All samples contained only one reduction peak at 400–650 °C. The reduction peak of VO_X/TiO_2 at the temperature of 482 °C corresponds to the transition of V^{5+} to V^{4+} and V^{4+} to V^{3+}, while in other samples, no reduction peak is observed at the corresponding position.[30] The reduction temperature of the cerium zirconium solid solution is 537 °C, which is caused by the conversion of Ce^{4+} to Ce^{3+}.[33] For the VO_X-loaded cerium–
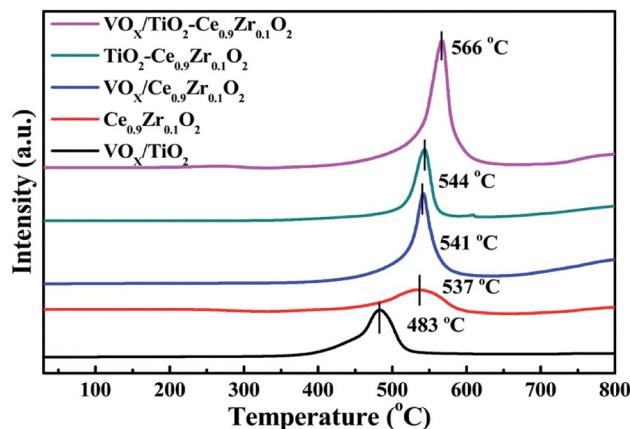

Fig. 3 H$_2$-TPR curve of catalysts and carriers.

zirconium solid solution, the reduction temperature is slightly higher, and the peak temperature is at 541 °C. It illustrates that there is a certain interaction between VO_X and $Ce_{0.9}Zr_{0.1}O_2$ inhibiting the conversion of V^{5+} to V^{4+} and a small amount of V^{4+} to V^{3+}, result in the shift to the higher temperature of the reduction peak. The reduction peak area is increased compared with $Ce_{0.9}Zr_{0.1}O_2$, which can be attributed to the effect of superposition of V^{5+}, V^{4+} and Ce^{4+} reduction peaks.[34] The reduction peak of TiO_2–$Ce_{0.9}Zr_{0.1}O_2$ is higher at 544 °C than that of $Ce_{0.9}Zr_{0.1}O_2$ alone, indicating the interaction between $Ce_{0.9}Zr_{0.1}O_2$ and TiO_2. While the reduction peak of the catalyst supported by TiO_2–$Ce_{0.9}Zr_{0.1}O_2$ is at 566 °C, which is higher than that of other catalysts and carriers. Similarly, the presence of the $Ce_{0.9}Zr_{0.1}O_2$ coating interacts strongly with the surface VO_X of the support, inhibiting the reduction process of VO_X. The larger reduction peak is the result of the superposition of Ce^{4+} to Ce^{3+}, V^{5+} to V^{4+} and V^{4+} to V^{3+}.

The hydrogen consumption of the samples are listed in Table 2. Since only Ce^{4+} on the surface is reduced, Ce of the internal bulk phase cannot be reduced in this temperature range of 400–650 °C, so the hydrogen consumption of $Ce_{0.9}Zr_{0.1}O_2$ is the least. For TiO_2–$Ce_{0.9}Zr_{0.1}O_2$, the specific surface area of $Ce_{0.9}Zr_{0.1}O_2$ is increased due to the formation of the core–shell structure, and more Ce is exposed and reduced, and the hydrogen consumption is significantly increased. TiO_2 is not reduced in the range of 50–800 °C, and all the hydrogen consumption of VO_X/TiO_2 belongs to the reduction of VO_X. By comparing the hydrogen consumption between the VO_X-loaded

Table 1 Specific surface area, pore volume, pore size, of the catalysts

Samples	SSA (cm^2 g^{-1})	PV (cm^3 g^{-1})	PS (nm)
TiO_2	114	0.42	9
VO_X/TiO_2	72	0.04	1
$Ce_{0.9}Zr_{0.1}O_2$	56	0.03	1
$VO_X/Ce_{0.9}Zr_{0.1}O_2$	57	0.26	9
TiO_2–$Ce_{0.9}Zr_{0.1}O_2$	74	0.04	1
VO_X/TiO_2–$Ce_{0.9}Zr_{0.1}O_2$	65	0.03	1

Table 2 The hydrogen consumption of samples

Samples	Hydrogen consumption (μmol g^{-1})
VO_X/TiO_2–$Ce_{0.9}Zr_{0.1}O_2$	163.5
TiO_2–$Ce_{0.9}Zr_{0.1}O_2$	87.8
$VO_X/Ce_{0.9}Zr_{0.1}O_2$	136.5
$Ce_{0.9}Zr_{0.1}O_2$	50.0
VO_X/TiO_2	96.2

catalyst and the support, we can confirm our previous inference about the superposition of the reduction peaks.

NH$_3$-TPD and Py-IR Analysis

In order to compare the number of surface acidic sites of several samples, we analyzed them with NH$_3$-TPD and showed the test results in Fig. 4. The desorption peak of NH$_3$ adsorbed physically on the surface of the catalyst is before 100 °C, and the desorption range at 100–200 °C, 200–400 °C and 400–500 °C correspond to weak acidic sites, medium strong acidic sites and strong acidic sites on the catalyst surface, respectively. TiO$_2$ and VO$_X$/TiO$_2$ mainly provide weak acid sites and a small amount of medium acid sites, Ce$_{0.9}$Zr$_{0.1}$O$_2$, VO$_X$/Ce$_{0.9}$Zr$_{0.1}$O$_2$ and TiO$_2$–Ce$_{0.9}$Zr$_{0.1}$O$_2$ can provide a small amount of strong acidic sites. The VO$_X$/TiO$_2$–Ce$_{0.9}$Zr$_{0.1}$O$_2$ catalyst has desorption peaks throughout the temperature range, indicating that the catalyst can provide three types of acidic sites.

VO$_X$/TiO$_2$–Ce$_{0.9}$Zr$_{0.1}$O$_2$ has the largest amount of NH$_3$ desorption (Table 3), indicating that the sample has the best ability to adsorb NH$_3$. This region can be thought of as VO$_X$ and TiO$_2$–Ce$_{0.9}$Zr$_{0.1}$O$_2$ together to provide weak, medium and strong acidic sites. The catalyst has a prominent ability to adsorb NH$_3$ and has more medium and strong acidic sites, thus the catalyst can exhibit the best catalytic activity and thermal stability.

Acid site type analysis was carried out at different temperatures for different catalysts and carriers. The Py-IR spectrum is shown in Fig. 5. The wave number corresponds to Lewis acid at 1437 cm^{-1} and 1597 cm^{-1}, and 1580 cm^{-1} and 1633 cm^{-1} correspond to Brønsted acid and the ratio of Brønsted acid to Lewis acid (B/L) is listed in Table 3.[35–37] According to studies by Li and Liu et al., anatase TiO$_2$ can only provide L acidic sites.[38,39] Compared with other samples containing TiO$_2$, the peak area of TiO$_2$ is smaller and the wave number is slightly higher. It can be considered that the peak of VO$_X$/TiO$_2$ is a result of superposition of VO$_X$ and TiO$_2$ peaks. Based on the special structure formed by Ce$_{0.9}$Zr$_{0.1}$O$_2$ and TiO$_2$, the TiO$_2$ core is mainly encapsulated in the Ce$_{0.9}$Zr$_{0.1}$O$_2$ shell. Although the medium acidic sites and strong acidic sites on the surface of Ce$_{0.9}$Zr$_{0.1}$O$_2$ are increased, it does not provide too much weak acidic sites (Fig. 4). Therefore,

Table 3 B/L and NH$_3$ desorption of different samples

Samples	B/L	Amount of NH$_3$ desorption (μmol g^{-1})
VO$_X$/TiO$_2$–Ce$_{0.9}$Zr$_{0.1}$O$_2$	0.53	462.4
TiO$_2$–Ce$_{0.9}$Zr$_{0.1}$O$_2$	0.86	244.5
VO$_X$/Ce$_{0.9}$Zr$_{0.1}$O$_2$	0.47	122.7
Ce$_{0.9}$Zr$_{0.1}$O$_2$	0.88	148.3
VO$_X$/TiO$_2$	0.76	401.3
TiO$_2$	—	350.4

the properties of providing weak acidic sites are not apparent in the samples of the core–shell structure. The largest B/L ratio is 0.88 that belongs to Ce$_{0.9}$Zr$_{0.1}$O$_2$. Ce$_{0.9}$Zr$_{0.1}$O$_2$ forms a core–shell structure with TiO$_2$, it also has a large B/L ratio. However, due to the loading of VO$_X$, the ratio of B/L is significantly reduced, indicating that the loading of VO$_X$ can provide more L acid sites. VO$_X$/TiO$_2$–Ce$_{0.9}$Zr$_{0.1}$O$_2$ catalyst has the largest acid area. There is interaction between the core–shell structure and the active component, which increases the number of acidic sites on the surface and is more conducive to the adsorption of NH$_3$ resulting in better catalytic activity of the catalyst.

In order to specifically explore the acid site composition of the surface of VO$_X$/TiO$_2$–Ce$_{0.9}$Zr$_{0.1}$O$_2$ catalyst, we performed Py-IR desorption analysis at different temperatures, and the spectrum is shown in Fig. 6. With the increase of the temperature desorption of weakly acidic sites combined with pyridine, and the characteristic peak area of acidic sites is decreasing. Due to the temperature rise, the increase of the vibration frequency of the in-plane ring deformation of pyridine combined with the medium acid sites and the strong acidic sites causes the characteristic peak to continuously move toward the high wavenumber. When the temperature reaches 150 °C, the adsorption peak attributed to the B acidic site disappears completely, and when the temperature reaches 300 °C, the characteristic adsorption peak of the L acidic site disappears, indicating that the L acidic site is the main role in the reaction process. For medium acid and strong acid sites, the temperature at which they desorb pyridine is relatively high. The presence of
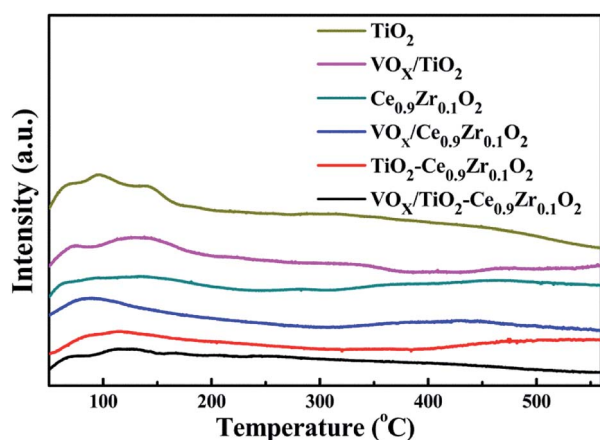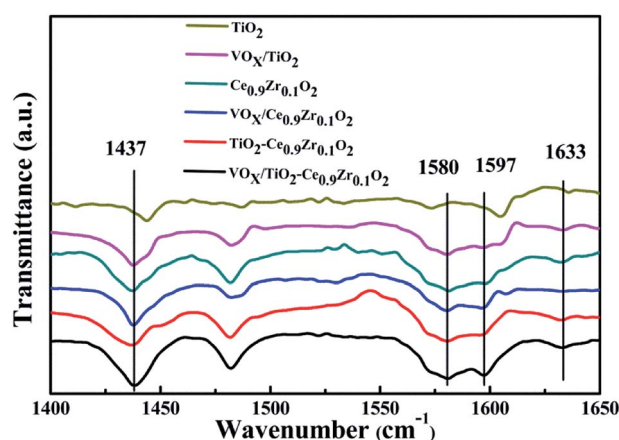

Fig. 4 NH$_3$-TPD curves of different samples.

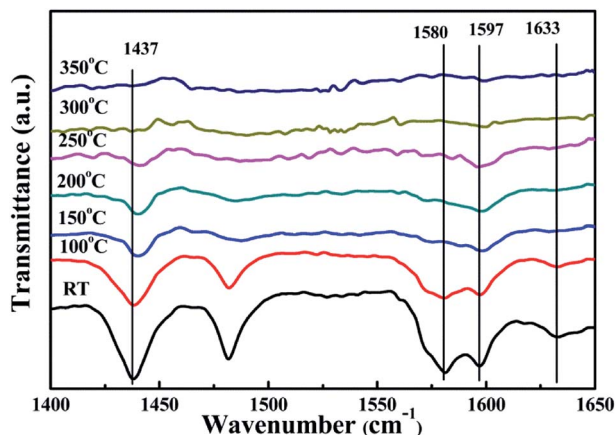**Fig. 5** Py-IR spectra of different samples.

Fig. 6 Py-IR spectra of VO_X/TiO_2–$Ce_{0.9}Zr_{0.1}O_2$ at different temperatures.

a medium acid and a strong acid site is a major factor in the relatively stable activity of the catalyst at higher temperatures.

XPS analysis

To investigate the chemical states of the elements in the near surface region of the catalyst samples, X-ray photoelectron spectroscopy (XPS) analysis was performed. All binding energies were referenced to the C 1s line at 284.8 eV. Table 4 is the calculated value of bulk compositions and the surface atomic ratios of different samples, for samples with a core–shell structure, the shell structure is relatively thin, and/or the incomplete coating, while the photoelectrons excite the electrons of the $Ce_{0.9}Zr_{0.1}O_2$ shell structure, some of the electrons of Ti are also excited, the ratio of Ce and Zr to Ti is close to 1.5 : 1. It is quite different from the calculated ratio in the core–shell structure, indicating that the solid solution is not simply mixed with TiO_2. The Zr atom has a relatively stable atomic ratio, which is consistent with the study by Yao et al.[40] Although we could not confirm the existence of V element in XRD and HRTEM, the existence of V atom was found in XPS detection, which indicates that V element is supported on the carrier. It should be noted that for VO_X-loaded catalysts, the atomic ratio of the surface V element is much higher than that of the bulk composition, because the V element is mainly supported on the surface of the carrier, and the high content of the V element on the surface is favorable for the NH_3-SCR reaction of NO.

The spectra of V 2p, O 1s, Ce 3d, Ti 2p and Zr 3d are given in Fig. 7, and the relative contents of different valence elements are listed in Table 5. Fig. 7a shows the V 2p photoelectron spectroscopy of different catalyst surfaces. The vanadium element is mainly present on the surface of the catalyst in the valence state of V^{5+} ($2p_{3/2}$) and V^{4+} ($2p_{3/2}$), and the corresponding binding energy is 517.3 eV and 516.3 eV, respectively.[41] The binding energy of V^{3+} ($2p_{3/2}$) is 515.5 eV.[42,43] The content of V^{3+} of $Ce_{0.9}Zr_{0.1}O_2$ and TiO_2 as carrier is small, while the content of V^{3+} in TiO_2–$Ce_{0.9}Zr_{0.1}O_2$ carrier is increased, and the content of V^{4+} is increased at the same time. Combined with the results of the H_2-TPR test, we speculate that this result is attributed to the interaction between $Ce_{0.9}Zr_{0.1}O_2$ and TiO_2, which increases the oxygen vacancies in the carrier, and the V element is supported on the surface of the core–shell structure carrier in a lower valence state. Due to the higher proportion of the V element on the surface and the presence of more low valence states V element, the catalyst has a higher catalytic activity.[29,31]

The results of XPS spectrum fitting of O 1s are shown in Fig. 7b, where the peak corresponding to lattice oxygen (O^{2-}) at 529.7 eV is expressed as O_β, and the binding energy is 531.4 eV corresponding to chemisorbed oxygen (O_2^{2-}, O^-), expressed as O_α.[44] For different carriers, the loading of VO_X will reduce the content of O_α, which may be because the loading of VO_X occupies the position of the support surface where the oxygen can be chemically adsorbed, resulting in a decrease in the O_α content of the catalyst surface after the loading. It is worth noted that $Ce_{0.9}Zr_{0.1}O_2$ has the lowest O_β binding energy, indicating that it has the best O migration ability. When VO_X is loaded or forms a core–shell structure with TiO_2, it will affect the migration ability of O_β. For TiO_2–$Ce_{0.9}Zr_{0.1}O_2$ and VO_X/TiO_2–$Ce_{0.9}Zr_{0.1}O_2$, a peak of –OH is generated at 530.2 eV, which may be formed by the adsorption of O_2 and H_2O by oxygen vacancies.[45–47] Due to the loading of VO_X, a small amount of oxygen vacancies is supplemented by VO_X, and the peak belonging to the –OH and O_α were reduced in VO_X/TiO_2–$Ce_{0.9}Zr_{0.1}O_2$ catalyst.

Fig. 7c shows the XPS spectrum of Ce 3d. According to previous studies,[18,48] the XPS spectrum of Ce 3d can be fitted to 8 peaks: where 'v' represents the $3d_{5/2}$ orbital and 'u' represents the $3d_{3/2}$ orbital. The peaks of u_1 and v_1 can be assigned to Ce^{3+}, and the other peaks are related to Ce^{4+}. The presence of Ce^{3+} causes charge imbalance and forms oxygen vacancies, which is favorable for the formation of surface chemisorbed oxygen.

Table 4 The calculated value of bulk compositions and surface atomic ratio of catalysts

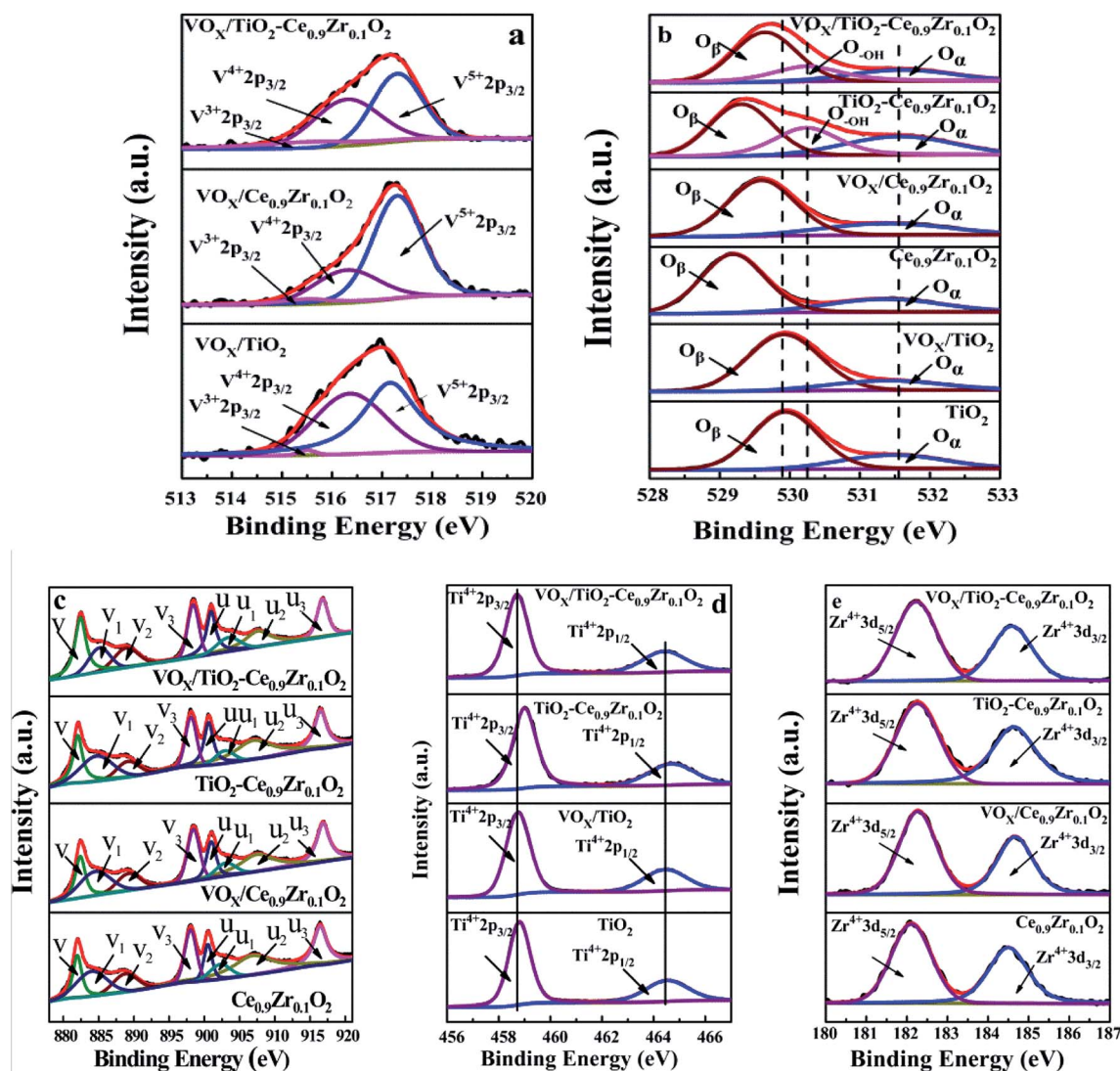| Catalysts	Calculated value of bulk compositions (%)				Surface atomic ratio (%)				
	V	Ce	Ti	Zr	V	O	Ce	Ti	Zr
VO_X/TiO_2–$Ce_{0.9}Zr_{0.1}O_2$	4.03	43.19	47.98	4.80	21.00	59.12	8.87	8.07	2.94
TiO_2–$Ce_{0.9}Zr_{0.1}O_2$	—	45.00	50.00	5.00	—	76.01	11.56	9.13	3.30
$VO_X/Ce_{0.9}Zr_{0.1}O_2$	5.38	85.16	—	9.46	20.95	63.21	12.68	—	3.16
$Ce_{0.9}Zr_{0.1}O_2$	—	90.00	—	10.00	—	78.49	17.92	—	3.59
VO_X/TiO_2	2.65	—	97.35	—	21.21	56.02	—	22.77	—
TiO_2	—	—	100	—	—	70.79	–	29.21	—

Fig. 7 XPS spectra of catalysts ((a) V 2p, (b) O 1s, (c) Ce 3d, (d) Ti 2p, (e) Zr 3d).

By comparing the existence of Ce in different samples, it can be found that the content of Ce^{3+} in $VO_X/TiO_2-Ce_{0.9}Zr_{0.1}O_2$ catalyst is reduced, and expect for v_2, the binding energies of Ce 3d in $VO_X/TiO_2-Ce_{0.9}Zr_{0.1}O_2$ are higher than those of $TiO_2-Ce_{0.9}Zr_{0.1}O_2$. Combined with the change in the valence state of the V element, we speculate that it may be that the loading VO_X weaken the

interaction between $Ce_{0.9}Zr_{0.1}O_2$ and TiO_2 and supplements the oxygen vacancies, resulting in a decrease in the content of Ce^{3+}, but an increase in the content of V^{3+} and V^{4+}.[49]

Fig. 7d is the XPS spectrum of Ti 2p, where 464.4 eV is the binding energy of Ti^{4+} $2p_{1/2}$ and 458.7 eV is the binding energy of Ti^{4+} $2p_{3/2}$. For $TiO_2-Ce_{0.9}Zr_{0.1}O_2$, the binding energy of Ti is

Table 5 Relative content of each element in different catalysts (%)

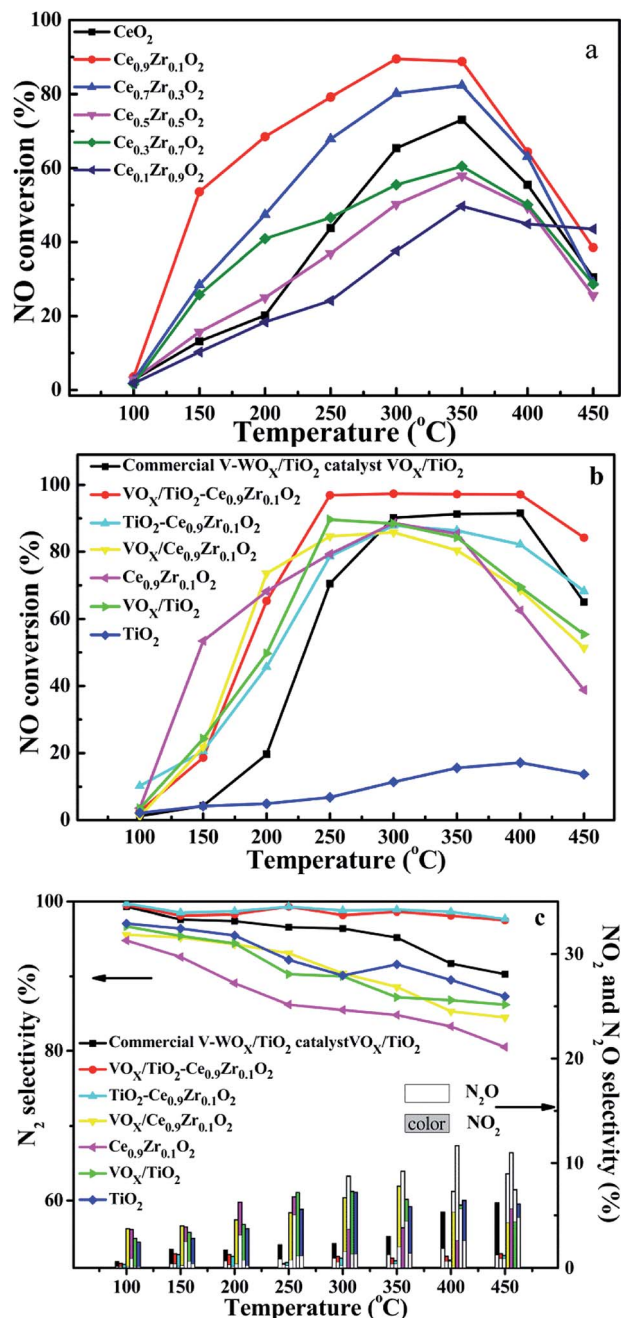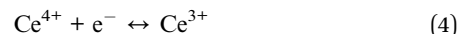| Catalysts	V 2p		O 1s		Ce 3d		
	$V^{3+} + V^{4+}$	V^{5+}	O_α	O_β	O_{-OH}	Ce^{3+}	Ce^{4+}
$VO_X/TiO_2-Ce_{0.9}Zr_{0.1}O_2$	54.61	45.39	20.47	56.09	23.44	18.25	81.75
$TiO_2-Ce_{0.9}Zr_{0.1}O_2$	—	—	27.24	45.13	27.63	21.18	78.82
$VO_X/Ce_{0.9}Zr_{0.1}O_2$	31.28	68.72	27.47	72.53	—	21.72	78.28
$Ce_{0.9}Zr_{0.1}O_2$	—	—	33.52	66.48	—	21.46	78.54
VO_X/TiO_2	43.69	56.31	20.49	79.51	—	—	—
TiO_2	—	—	26.32	73.68	—	—	—

Fig. 8 NO conversion curve of $Ce_xZr_{1-x}O_2$ (a), NO conversion and selectivity of catalysts and carriers (b and c).

shifted. The reason for this phenomenon is related to the interaction between $Ce_{0.9}Zr_{0.1}O_2$ and TiO_2, which may cause lattice distortion of TiO_2 (it is reflected in the XRD spectrum).[41] It can provide more oxygen vacancies. Due to the load of VO_X, while supplementing the oxygen vacancies, the existence of higher binding energy Ti is weakened as well. Therefore, the higher binding energy of Ti in $VO_X/TiO_2–Ce_{0.9}Zr_{0.1}O_2$ catalyst is not obvious. However, the loaded VO_X can provide more active sites.
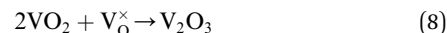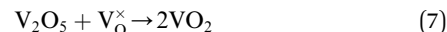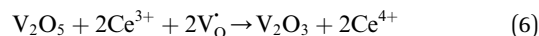
For the XPS of Zr (Fig. 7e), Zr mainly exists as +4 valence ion, and the addition of Zr^{4+} is beneficial to the generation of oxygen

vacancies. The increase of oxygen vacancies has a great influence on the thermal stability of the catalyst carrier. The strong interaction between the $TiO_2–Ce_{0.9}Zr_{0.1}O_2$ support with core–shell structure increases the high temperature stability of the composite supported catalyst, which also explains the higher activity of the catalyst at higher temperatures.[50]

Combined with the results of the above characterization, we can confirm that after the preparation of $TiO_2–Ce_{0.9}Zr_{0.1}O_2$ core–shell structure, the electrons in Ce–O–Ti shift to Ce due to the interaction between TiO_2 and $Ce_{0.9}Zr_{0.1}O_2$.[49,51] The binding energy of Ti^{4+} becomes higher and the electron density around Ce increases. The electron cloud density of Ce increase, and the migration ability of O in $Ce_{0.9}Zr_{0.1}O_2$ is enhanced, which is beneficial to the generation of oxygen vacancies. The content of Ce^{3+} and chemisorbed oxygen indirectly reflects the amount of oxygen vacancies.[52] It is generally believed that there are three types of oxygen vacancies ($V_O^\times, V_O^\bullet$ and $V_O^{\bullet\bullet}$), which are inseparable from the reactions (1)–(3).[45,53–55] Oxygen vacancies adsorb oxygen and dissociate O_2 into oxygen atoms. Since oxygen atoms have high activity, they can adsorb substances such as water to form –OH. Due to the presence of oxygen vacancies, Ce can be converted from the +4 valence to the +3 valence (reaction (4)).

$$V_O^\times \leftrightarrow V_O^\bullet + e^- \tag{1}$$

$$V_O^\times \leftrightarrow V_O^{\bullet\bullet} + 2e^- \tag{2}$$

$$V_O^\bullet \leftrightarrow V_O^{\bullet\bullet} + e^- \tag{3}$$

$$Ce^{4+} + e^- \leftrightarrow Ce^{3+} \tag{4}$$

When VO_X is loaded, an interaction occurs between the active component and the carrier, electron transfer occurs between Ce^{3+} and VO_X, and oxygen vacancies are replenished, and the following reactions may occur during the preparation process (reactions (5)–(8)):

$$V_2O_5 + 2Ce^{3+} + V_O^{\bullet\bullet} \rightarrow 2VO_2 + 2Ce^{4+} \tag{5}$$

$$V_2O_5 + 2Ce^{3+} + 2V_O^\bullet \rightarrow V_2O_3 + 2Ce^{4+} \tag{6}$$

$$V_2O_5 + V_O^\times \rightarrow 2VO_2 \tag{7}$$

$$2VO_2 + V_O^\times \rightarrow V_2O_3 \tag{8}$$

However, this reaction is difficult to accomplish in $VO_X/Ce_{0.9}Zr_{0.1}O_2$ catalyst. The oxygen vacancies of $Ce_{0.9}Zr_{0.1}O_2$ coated on the surface of TiO_2 were supplemented. The intensity of the diffraction peak in the XRD spectrum of the catalyst is enhanced, and the peak shape is sharper the presence of more low-valence V elements requires higher temperatures due to the increased number of V^{4+} to V^{3+} conversions, resulting in a shift in the peak temperature of the H_2-TPR (Fig. 3). In summary, the increased V^{4+} and V^{3+} content in VO_X improves catalytic activity. The interaction between the support and the active component is responsible for the better thermal stability of the catalyst.

Catalyst activity analysis

Fig. 8a is a graph showing the activity of solid solution of different cerium–zirconium ratios. $Ce_{0.9}Zr_{0.1}O_2$ exhibits better catalytic activity, while the catalytic activity of $Ce_{0.1}Zr_{0.9}O_2$ is the worst among all solid solutions at the range of 100–400 °C, although it is better than others at 450 °C. The above results indicate that proper zirconium doping is beneficial to improve the activity and increase the thermal stability of the catalysts. Based on the activity of the cerium–zirconium solid solution catalyst, we selected $Ce_{0.9}Zr_{0.1}O_2$ as the shell structure component to prepare core–shell carrier.

Fig. 8b and c show NO conversion curves and selectivity curves for different VO_X supported catalysts and their supports. Different colors are used to represent different samples, the line chart represents N_2 selectivity, and the histogram shows the selectivity of N_2O and NO_2 in Fig. 8c. Under the condition of GSHV = 40 000 h^{-1}, $Ce_{0.9}Zr_{0.1}O_2$ and $VO_X/Ce_{0.9}Zr_{0.1}O_2$ showed higher activity before 250 °C, which may be because the oxygen vacancies and the redox of Ce^{3+} are the main catalytic sites at low temperature. The VO_X site is effectively attached to the surface of the support and the redox properties of the catalysts determine the catalytic activity, rather than the Lewis and Brønsted surface acidic sites in the catalytic system.[15,16] After 250 °C, VO_X/TiO_2–$Ce_{0.9}Zr_{0.1}O_2$ showed excellent catalytic activity and maintained excellent selectivity and thermal stability with NO conversion rate > 97%, N_2 selectivity > 97.5% and temperature window is 250–400 °C, which is inseparable from the existence of low-valence V and medium – strong acidic sites. The former is beneficial to increase the activity of the catalyst, and the latter is advantageous for improving the thermal stability of the catalyst. Compared with commercial catalysts, VO_X/TiO_2–$Ce_{0.9}Zr_{0.1}O_2$ has the higher NO conversion and N_2 selectivity, wider temperature window and better thermal stability.[31] It is noteworthy that TiO_2–$Ce_{0.9}Zr_{0.1}O_2$ also exhibits a high N_2 selectivity, although its catalytic properties is not particularly excellent compared to the commercial catalysts and VO_X/TiO_2–$Ce_{0.9}Zr_{0.1}$. It indicates that the higher selectivity of N_2 is derived from the TiO_2–$Ce_{0.9}Zr_{0.1}O_2$ core–shell structure carrier.

Conclusion

In summary, we prepared a TiO_2–$Ce_{0.9}Zr_{0.1}O_2$ support with core–shell structure by precipitation method, which may not be completely coated. Owing to the interaction between TiO_2 and $Ce_{0.9}Zr_{0.1}O_2$, the carrier has lower lattice oxygen content and a large number of active oxygen vacancies that can adsorb O_2 and H_2O in the air, which is the reason for the formation of –OH on the surface of the carrier. Due to the presence of $Ce_{0.9}Zr_{0.1}O_2$ coating layer, VO_X/TiO_2–$Ce_{0.9}Zr_{0.1}O_2$ catalyst exhibits better catalytic properties. After loading VO_X, the decrease of Ce^{3+} and the oxygen vacancies content in the catalyst is due to the supplement of oxygen vacancies and the electron transfer between high valence state V and Ce^{3+}. The presence of the low-valent V is more favourable for the NH_3-SCR reaction. At the same time, the VO_X/TiO_2–$Ce_{0.9}Zr_{0.1}O_2$ catalyst contains more acidic sites, especially medium-strong acid sites. It is beneficial to the adsorption of the reaction gas NH_3 on the catalyst surface and increased thermal stability. Compared with the commercial catalysts currently used on the market, both conversion rate and selectivity are superior, as well as better thermal stability and a wider temperature window, which provides ideas for the development of more superior catalysts in the future.

Conflicts of interest

There are no conflicts to declare.

Acknowledgements

References

1 X. Liu, X. Wu, T. Xu, W. Duan, Z. Si and R. Ran, *Chin. J. Catal.*, 2016, **37**(8), 1340–1346.

2 X. T. Zhao, L. Mao and G. J. Dong, *Catalysts*, 2018, **8**(2), 76–89.

3 F. Lónyi, H. E. Solt, Z. Pászti and J. Valyon, *Appl. Catal., B*, 2014, **150–151**(18), 218–229.

4 Z. Ma, X. Wu, Z. Si, W. Duan, M. Jing and T. Xu, *Appl. Catal., B*, 2015, **179**, 380–394.

5 B. X. Shen, F. M. Wang, B. Zhao, Y. W. Li and Y. Y. Wang, *J. Ind. Eng. Chem.*, 2016, **33**, 262–269.

6 C. E. Quincoces, A. K. D. Figueiredo, A. Lavat and G. G. María, *React. Kinet., Mech. Catal.*, 2000, **71**(2), 253–262.

7 N. J. Fang, J. X. Guo, S. Shu, H. D. Luo, Y. H. Chu and J. J. Li, *Chem. Eng. J.*, 2017, **325**(1), 114–123.

8 S. Prodinger, M. A. Derewinski, Y. L. Wang, N. M. Washton, E. D. Walter, J. Szanyi, F. Gao, Y. Wang and C. H. F. Peden, *Appl. Catal., B*, 2017, **201**, 461–469.

9 X. Gao, Y. Jiang, Y. C. Fu, Y. Zhong, Z. Y. Luo and K. F. Cen, *Catal. Commun.*, 2010, **11**(5), 465–469.

10 R. T. Guo, Y. Zhou, W. G. Pan, J. N. Hong, W. L. Zhen, Q. Jin, C. G. Ding and S. Y. Guo, *J. Ind. Eng. Chem.*, 2013, **19**(6), 2022–2025.

11 T. H. Vuong, J. Radnik, M. Schneider, H. Atia, U. Armbruster and A. Brückner, *Catal. Commun.*, 2016, **84**(5), 171–174.

12 F. Y. Gao, X. L. Tang, H. H. Yi, J. Y. Li, S. Z. Zhao, J. G. Wang, C. Chu and C. L. Li, *Chem. Eng. J.*, 2017, **317**(1), 20–31.

13 L. K. Zhao, C. T. Li, J. Zhang, X. N. Zhang, F. M. Zhan, J. F. Ma, Y. E. Xie and G. M. Zeng, *Fuel*, 2015, **153**(1), 361–369.

14 P. Li, Y. Xin, Q. Li, Z. P. Wang, Z. L. Zhang and L. R. Zheng, *Environ. Sci. Technol.*, 2012, **46**(17), 9600–9605.

15 T. H. Vuong, J. Radnik, J. Rabeah, U. Bentrup, M. Schneider, H. Atia, U. Armbruster, W. Grünert and A. Brückner, *ACS Catal.*, 2017, **7**(3), 1693–1705.

16 T. H. Vuong, J. Radnik, E. Kondratenko, M. Schneider, U. Armbruster and A. Brückner, *Appl. Catal., B*, 2016, **197**(15), 159–167.

17 Z. G. Li, J. H. Li, S. X. Liu, X. N. Ren, J. Ma, W. K. Su and Y. Peng, *Catal. Today*, 2015, **258**(2), 11–16.

18 S. H. Li, B. C. Huang and C. L. Yu, *Catal. Commun.*, 2019, **98**(10), 47–51.

19 S. L. Zhang and Q. Zhong, *J. Solid State Chem.*, 2015, **221**, 49–56.

20 P. G. W. A. Kompio, A. Brückner, F. Hipler, E. Löffler and W. Grünert, *J. Catal.*, 2012, **286**, 237–247.

21 D. N. Corra, J. M. D. E. Slilva, E. B. Santos, F. A. Sigoli, A. G. Souza and I. O. Mazali, *J. Phys. Chem. C*, 2011, **115**(21), 10380–10387.

22 S. D. Zhao, J. R. Chen, Y. F. Liu, Y. J. Jiang, C. G. Jiang, Z. L. Yin, Y. G. Xiao and S. S. Cao, *Chem. Eng. J.*, 2019, **367**(1), 249–259.

23 G. N. Li, B. H. Wu and L. Li, *J. Mol. Catal. A: Chem.*, 2016, **424**(1), 304–310.

24 M. Piumetti, S. Bensaid, N. Russo and D. Fino, *Appl. Catal., B*, 2016, **180**, 271–282.

25 Z. H. Ren, P. Wang, J. Kong, M. J. Wang and L. P. Chang, *J. Energy Chem.*, 2017, **26**(4), 647–654.

26 M. Piumetti, S. Bensaid, D. Fino and N. Russo, *Appl. Catal., B*, 2016, **197**(15), 35–46.

27 L. Zhang, J. F. Sun, L. L. Li, S. M. Ran, G. X. Li, C. J. Li, C. Y. Ge and D. Lin, *Ind. Eng. Chem. Res.*, 2018, **57**(2), 490–497.

28 W. Y. Zhou, J. Y. Liu, J. Y. Song, J. J. Li, J. H. Liu and X. J. Huang, *Anal. Chem.*, 2017, **8**(96), 3386–3394.

29 J. X. Hao, S. L. Peng, H. Q. Li, S. Dang, T. F. Qin, Y. X. Wen, J. J. Huang, F. Ma, D. Q. Gao, F. Li and G. Z. Cao, *J. Mater. Chem. A*, 2018, **6**, 16094–16100.

30 J. W. Liu, Q. Sun, Y. C. Fu and J. Y. Shen, *J. Colloid Interface Sci.*, 2009, **335**(2), 216–221.

31 T. Boningari, R. Koirala and P. G. Smirniotis, *Appl. Catal., B*, 2013, **140–141**, 289–298.

32 L. Chen, J. H. Li and M. F. Ge, *Chem. Eng. J.*, 2011, **170**(2–3), 531–537.

33 P. Maitarad, D. S. Zhang, R. H. Gao, L. Y. Shi, H. R. Li, L. Huang, T. Ruangrotmongkol and J. P. Zhang, *J. Phys. Chem. C*, 2013, **117**(19), 9999–10006.

34 A. A. H. Elbadawi, M. Y. Khan, M. R. Quddus, S. A. Razzak and M. Hossain, *AIChE J.*, 2017, **63**(1), 130–138.

35 C. A. Emeis, *J. Catal.*, 1993, **141**(2), 347–354.

36 E. P. Parry, *J. Catal.*, 1963, **2**(5), 371–379.

37 Y. Liu, T. T. Gu, Y. Wang, X. L. Weng and Z. B. Wu, *Catal. Commun.*, 2012, **18**, 106–109.

38 L. C. Li, H. Q. Yue, T. Ji, W. Li, X. J. Zhao, L. Wang, J. She, X. L. Gu and X. B. Li, *Appl. Catal., A*, 2019, **574**(2), 25–32.

39 F. Liu, T. F. Wang, Y. Y. Zheng and J. F. Wang, *J. Catal.*, 2019, **355**(1), 17–25.

40 X. J. Yao, L. Chen, J. Gao, Y. Chen, M. Tian, F. M. Yang, J. F. Sun, C. J. Tang and L. Dong, *Chem. Eng. J.*, 2019, **369**(1), 46–56.

41 M. A. Eberhardt, A. Proctor, M. Houalla and D. M. Hercules, *J. Catal.*, 1996, **160**(1), 27–34.

42 M. Demeter, M. Neumann and W. Reichelt, *Surf. Sci.*, 2000, **454**(12), 41–44.

43 G. Silversmit, D. Depla, H. Poelman, G. B. Marin and R. D. Gryse, *J. Electron Spectrosc. Relat. Phenom.*, 2004, **135**(2–3), 167–175.

44 M. L. Abel, A. Carley, J. F. Watts, E. Hryha, E. Rutqvist and L. Nyborg, *Surf. Interface Anal.*, 2012, **44**(8), 1022–1025.

45 Z. Y. Xiu, Z. P. Xing, Z. Z. Li, X. Y. Wu, X. Yan, M. Q. Hu, Y. Gao, S. L. Yang and W. Zhou, *Mater. Res. Bull.*, 2018, **100**, 191–197.

46 H. U. Khan and I. K. Swati, *Ind. Eng. Chem. Res.*, 2016, **55**(23), 6619–6633.

47 H. Li, Z. Chen, C. K. Tsang, Z. Li, X. Ran, C. Lee, B. Nie, L. X. Zheng, T. F. Hung and J. Lu, *J. Mater. Chem. A*, 2013, **2**(1), 229–236.

48 R. T. Guo, Q. L. Chen, H. L. Ding, Q. S. Wang, W. G. Pan, N. Z. Yang and C. Z. Lu, *Catal. Commun.*, 2015, **69**(5), 165–169.

49 T. M. Wandre, P. N. Gaikwad, A. S. Tapase, K. M. Garadkar, S. A. Vanalakar, P. D. Lokhande, R. Sasikala and P. P. Hankare, *J. Mater. Sci.: Mater. Electron.*, 2016, **27**(1), 825–833.

50 A. Kambolis, H. Matralis, A. Trovarelli and C. Papadopoulou, *Appl. Catal., A*, 2010, **377**(1), 16–26.

51 B. Yang, Z. Li, Q. Huang, M. D. Chen, L. L. Xu, Y. S. Shen and S. M. Zhu, *Chem. Eng. J.*, 2019, **360**(15), 990–1002.

52 L. R. Shah, B. Ali, H. Zhu, W. G. Wang, Y. Q. Song, H. W. Zhang, S. L. Shah and J. Q. Xiao, *J. Phys.: Condens. Matter*, 2009, **21**(48), 486004–486012.

53 R. D. Liu, H. Li, L. B. Duan, H. Shen, Q. Zhang and X. R. Zhao, *J. Alloys Compd.*, 2019, **789**(15), 1015–1021.

54 X. Y. Zhang, J. Q. Qin, Y. N. Xue, P. F. Yu, B. Zhang, L. M. Wang and R. P. Liu, *Sci. Rep.*, 2014, **4**, 4596–4603.

55 R. Fiorenza, M. Bellardita, T. Barakat, S. Scirè and L. Palmisano, *J. Photochem. Photobiol., A*, 2018, **352**(1), 25–34.